Science and Technology Indonesia
e-ISSN:2580-4391 *p*-ISSN:2580-4405
Vol. 10, No. 2, April 2025

Research Paper

Synthesis and Characterization of Co_3O_4 and ZnO Nanoparticles Based on Schiff Base Complexes as a Precursor to the Photocatalytic Photodegradation of Congo Red Dye

Shahad Qasim Raji[1], Ali Taleb Bader[1]*

[1]*Department of Chemistry, College of Science for Women, University of Babylon, Hilla, 51001, Iraq*
***Corresponding author**: wsc.ali.taleb@uobabylon.edu.iq

Abstract
The synthesis of $[Co(HBZAP)(OAC)_2]2H_2O$ and $[Zn(HBZAP)(OAC)_2]$ H_2O complexes was successfully performed through reflux in connection with the Schiff bases synthesized with metal salt acetate hydrate. Identification of the synthesized complexes was performed by Fourier transform infrared FTIR, UV-Vis, magnetic moment, ^1H, and ^{13}C-NMR spectroscopy and X-Ray diffraction XRD. These studies show the Schiff base ligand as bidentate due to oxygen from the phenolic group and nitrogen from the azomethane group for complexation with Co(II) and Zn(II), resulting in a tetrahedral configuration of the complexes around the metal ions. Conductivity measurements in DMSO demonstrated that none of the complexes would permit the conduction of electricity. Co_3O_4 and ZnO nanoparticles were synthesized from these Co(II) and Ni(II) complexes. FTIR and UV-Vis spectra, as well as FE-SEM images, were used to identify the synthesized nanostructures. These results show that the Co_3O_4 and ZnO nanoparticles have cubic and hexagonal systems, respectively. The average crystallite sizes of Co_3O_4 and ZnO are 36.5 and 31.9 nm, respectively. These nanoparticles show excellent photocatalytic activity when used under UV light to degrade Congo red dye in aqueous media for 120 minutes of 91.4% and 60.6%.

Keywords
Schiff Base, $[Co(HBZAP)(OAC)_2]2H_2O$ and $[Zn(HBZAP)(OAC)_2]$ H_2O Complexes, Co_3O_4, ZnO, Nanoparticles, Photocatalytic Activity

Received: 29 September 2024, Accepted: 31 January 2025
https://doi.org/10.26554/sti.2025.10.2.420-431

1. INTRODUCTION

Schiff base transition metal complexes have garnered significant attention recently due to their remarkable properties and diverse applications. These complexes exhibit various biological activities, including antibacterial, anti-inflammatory, antipyretic, antioxidant, and antiviral effects. Additionally, they serve as versatile catalysts in numerous chemical reactions, such as alkene halogenation, polymerization, ketone reduction, thionyl chloride reactions, Henry reactions, aldol reactions, and the oxidation of organic compounds. Owing to their extensive utility, Schiff bases represent a critically important class of compounds in pharmaceutical and medical sciences (Abass et al., 2020; Abdelrahman and Al-Farraj, 2022; Gaur et al., 2023).

Using Schiff base complexes to synthesize metal oxide nanoparticles (NPs) offers several advantages. First, Schiff bases can effectively stabilize metal ions in solution; hence, they can prevent the coalescence of metal ions and promote controlled nucleation in NP synthesis (Patil et al., 2020). Second, they can produce uniform NPs of certain shapes and sizes. This control over morphology is essential to tailoring the desired properties of the metal oxides. Finally, metal oxides prepared from Schiff bases usually possess improved catalytic activity due to the organic ligand, which is believed to modify the electronic and surface reactivity of the metal oxide (Mahadevi and Sumathi, 2023; Nassar et al., 2017).

Due to their ability to coordinate with numerous metal ions, Schiff base metal complexes have received wide attention in the literature for producing metal complexes with custom properties (Adaji et al., 2024). For example, several recent reports have demonstrated that Schiff base metal complexes can produce metal oxide NPs with small crystallite sizes, such as Co_3O_4, CuO, and NiO, using simple and inexpensive methods.

The significance of these nanomaterials lies in their broad application. For example, they can degrade roxarsone, adsorb secondary inorganic arsenic, detect acetone with high selectivity, act as the anode in Li-ion batteries, have antibacterial properties, or be used in the photocatalytic degradation of organic dyes (Abdelrahman and Al-Farraj, 2022). More recently, the use of coordination compounds as novel precursors for the synthesis of nanometer-sized metal oxides is one of the easiest and most practical routes because it eliminates the need for

special equipment and complex procedures and produces novel structures and high-purity by-products (Nwaiwu et al., 2024). Schiff base complexes have gained popularity as precursors for metal oxide NPs because they permit the controlled release of metal ions during the thermal decomposition step (Subhi et al., 2022).

Co_3O_4 and ZnO NPs obtained from Schiff base complexes possess improved physical adsorptions, which enhance photocatalytic activity. For example, Co_3O_4 and ZnO NPs synthesized from Schiff base complexes have improved the photodegradation of various dyes, such as Congo red (CR) and rhodamine B (Abass et al., 2020; Abdelrahman and Al-Farraj, 2022). ZnO has shown good activity as a photocatalyst for degrading organic dyes even in UV light; many researchers have confirmed this. In particular, the efficacy of ZnO against the degradation of dyes, including methyl orange, methylene blue, and CR, has been studied.

Co_3O_4 (cobalt (II,III) oxide) is a mixed-valence metal oxide consisting of Co^{2+} and Co^{3+} ions, giving it unique electronic and catalytic properties. There are tetrahedral and octahedral sites on the spinal structure. These structures give good stability and magnetic properties (Gaur et al., 2023; Nwaiwu et al., 2024; Singh and Major, 2016). Co_3O_4 is an antiferromagnetic material with a Neel temperature of roughly 40 K. Nevertheless, at room temperature, it functions as a paramagnetic material, which is beneficial to certain magnetic and electronic applications. It is a notable p-type semiconductor with a direct optical band gap of 2.44 eV, making it highly suitable for various applications, including biomedical imaging, cancer therapy, pharmacology, chemical sensing, catalysis, and semiconductor transistors. It finds applications in lithium-ion batteries, supercapacitors, and electrocatalysis because of its reversible redox reaction that increases energy storage (Naikoo et al., 2024; Zhu et al., 2008).

Zinc oxide (ZnO) is a binary compound in which zinc is in the +2-oxidation state (Zn^{2+}) while oxygen is in an oxidation state of -2 (O^{2-}). ZnO has a wurtzite structure at room temperature; this is the most stable form. This specific structure is characterized by hexagonal crystal symmetry and polar surfaces, producing piezoelectric and pyroelectric effects (Saeed et al., 2024). ZnO is an outstanding thinned semiconducting material with a direct wide band gap (3.3 eV) at room temperature. Thus, it is in the UV spectrum and can be utilized for optoelectronics, including UV LEDs, laser diodes, and solar cells. It possesses great stability, cost-efficiency, superior electrical conductivity, higher binding free energy (approximately 60 meV), and biocompatibility, which are outstanding features (Kumar et al., 2022). Because of its strong oxidative abilities and stability, ZnO is a very effective photocatalyst for the breakdown of organic pollutants through UV light. Zinc oxide NPs can play a significant role in degrading dyes, such as CR and methylene blue, during wastewater treatment. Known for their versatility, these NPs are used across various industries, including nanodiagnostics, nanocomposites, antimicrobial agents, antioxidants, paints, and coatings, due to their effective UV protection properties (Dao et al., 2023).

In this study, ^{13}C, ^{1}H-NMR, FTIR, and UV-Vis spectroscopy were used to describe the structure of the compounds. In addition, SEM and XRD were employed to examine the shape and structure of the as-prepared Co_3O_4 and ZnO NPs.

2. EXPERIMENTAL SECTION

2.1 Material

Materials used were 2-hydroxy benzaldehyde (99%, Merck, Germany), 4-aminophenol (98%, Merck), cobalt acetate tetrahydrate ($Co(CH_3COOH)_2 \cdot 4H_2O$), zinc acetate dihydrate ($Zn(CH_3COOH)_2.4H_2O$, 98%, BDH, England) and CR dye (analytical standard grade, Merck).

2.2 Instrument

A SMP30 digital melting point apparatus (Stuart), a 8400s FTIR spectrometer (Shimadzu), a 1700 UV-visible spectrophotometer with Lisper diffuse reflectance capability (Shimazu), a Bruker DMX-400 NMR spectrometer, a Shimadzu XRD-6000 X-ray diffractometer, and a TESCAN MIRA III FESEM were used in this work.

2.3 Methods

2.3.1 Synthesis of N-(2-Hydroxybenzylidene)-4-aminophenol (HBZAP)

A condensation reaction was used to synthesize the ligand, as illustrated in Figure 1. A round-bottom flask was preheated to 100°C and filled with a solution of 5-hydroxybenzaldehyde (3 mL) and p-aminophenol (3.05 g), which was dissolved in the same amount of ethanol and acetic acid. After 4 h of reflux, the mixture was cooled. The precipitate was recrystallized after vacuum filtration. We recrystallized 3.02 g (74%) of the solvent from ethanol under reduced pressure. The recrystallized product was collected and dried in a vacuum desiccator (Ashraf et al., 2011).

2.3.2 Synthesis of $[Co(HBZAP)(OAC)_2]2H_2O$ and $[Zn(HBZAP)(OAC)_2]$ H_2O Complexes

A similar protocol was used to prepare the metal-ion II complexes: two copper or zinc ion solutions, each containing 0.5 g (0.0023 mole) of metal-ion salt in 20 ml of ethanol, were prepared. During 5 hours of reflux, a hot ethanolic solution of the Schiff base ligand (1 g, 0.0046 mmol) was gradually added to each metal salt solution. The solutions were allowed to cool to room temperature, and the precipitates were filtered and washed with ethanol. The precipitates were then dried and weighed to determine the amount of metal-ion II, as shown in Figure 2.

2.3.3 Synthesis of Co_3O_4 and ZnO NPs

NPs of ZnO and Co_3O_4 in Figure 1 were produced by thermally decomposing the Schiff bases for 5 hours at 500°C (Al-Wasidi et al., 2022; Pushpanathan and Suresh Kumar, 2014).

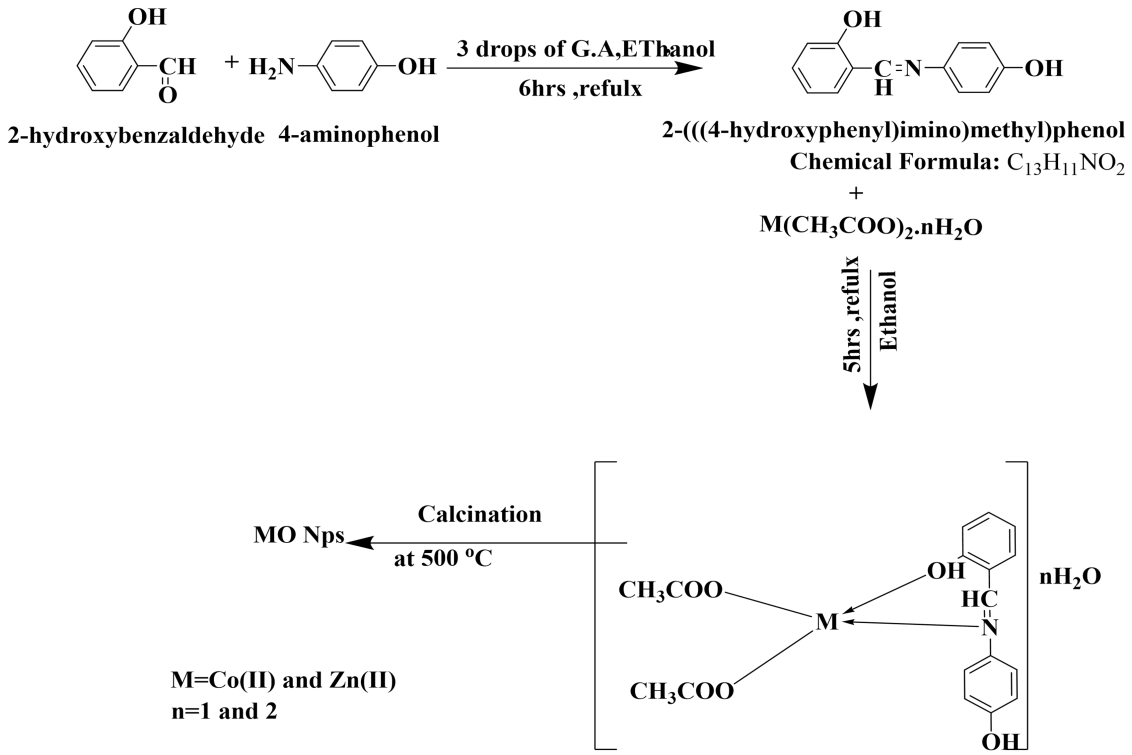

Figure 1. Syntheses of N-(2-Hydroxybenzylidene)-4-aminophenol (HBZAP) [Co(HBZAP)(OAC)$_2$]2H$_2$O, [Zn(HBZAP)(OAC)$_2$] H$_2$O and Metal Oxide NPs

2.3.4 Photocatalytic Degradation

The photocatalytic efficiency of the Co_3O_4 and ZnO NPs was evaluated for the degradation of CR dye under UV irradiation. The experiments were conducted in a 250-mL photoreactor equipped with a 125 W high-pressure mercury lamp (λ max = 365 nm). Before irradiation, the lamp was preheated for 10 min to stabilize its output. For each trial, 0.3 g of photocatalyst (Co_3O_4 or ZnO) was dispersed in 200 mL of CR solution (10 mg/L). To establish the adsorption-desorption equilibrium, the mixture was magnetically stirred in the dark for 10 min. Subsequently, the solution was transferred to the photoreactor, where continuous aeration (0.1 mL/min) was maintained via an air diffuser to ensure homogeneous mixing and oxygen saturation.

Aliquots were collected regularly, diluted appropriately, and analyzed using a UV-Vis spectrophotometer (Shimadzu UV mini-1240, Japan) at λ max = 663 nm (3-cm quartz cell). Calibration curves derived from standard solutions were used to quantify residual dye concentrations. The photodegradation efficiency (%) was calculated based on the relative decrease in absorbance, and the apparent pseudo-first-order rate constant (k) was determined using Equation (1) to assess the reaction kinetics.

$$PDE\% = \frac{A^0 - At}{A^0} \times 100\% \quad (1)$$

where:

A^0 denotes the initial reactant concentration at time t = 0.
At represents the reactant concentration at a defined irradiation time, t.
$PDE\%$ quantifies the percentage of degradation efficiency achiev ed through light-driven photocatalytic processes.

3. RESULTS AND DISCUSSION

3.1 Fourier Transform Infrared (FTIR) Spectroscopy Characterizations

3.1.1 Characterizations of Regents (2-Hydroxybenzaldehyde, p-Aminophenol) and N-(2-Hydroxybenzylidene)-4-Aminophenol (HBZAP)

The FTIR spectrum of a sample of 2-hydroxybenzaldehyde (also known as salicylaldehyde) in Figure 2 will show characteristic absorption bands related to the bonds in the molecule. The hydroxyl group in 2-hydroxybenzaldehyde can form intramolecular hydrogen bonds with the carbonyl group that shift and broaden the O−H stretch to lower wavenumbers. The broad absorption between 3182-3200 cm^{-1} indicates a hydroxyl group. The carbonyl stretch of the aldehyde is indicated by a strong band at 1664 cm^{-1}. Multiple peaks at 1400-1600 cm^{-1} relate to aromatic C=C stretching and at 3063 cm^{-1} for aromatic C−H stretching, confirming the aromatic nature of the compounds.

After analyzing the FTIR spectrum Figure 2 of para-aminop henol, the N−H stretching vibrations have two bands in the

3354-3294 cm^{-1} region because of symmetric and asymmetric stretching modes. In this case, the FTIR spectra of the ligand as showed in Figure 2 (N-(2-Hydroxybenzylidene)-4-aminophenol (HBZAP)) and the starting material were compared, and several differences were observed. The hydrogen bond between the NH and OH in the proposed structure agrees with the band at 3045 cm^{-1} corresponding to the υ(O−H) of the phenolic group (OH). The N−H stretch proves the presence of an OH/NH hydrogen bond intermolecularly, as there is no indication of the absorption bands (υOH at 3354 cm^{-1} of the phenolic group and υNH_2 at 3295 cm^{-1}) of 4-aminophenol. A new vibration band near 1631 cm^{-1}, corresponding to the υ(C=N) stretching mode, confirms the formation of the Schiff base ligand, L (Abdallah et al., 2009; Al-Wasidi et al., 2022; Pavia et al., 2014).

3.1.2 FTIR $[Co(HBZAP)(OAC)_2]2H_2O$,$[Zn(HBZAP)(OAC)_2]$ H_2O and Metal Oxide NPs

In the study of various metal–ion complexes, the structures of the complexes can be effectively determined by comparing the spectra of the free ligand (L) with those of the corresponding complexes. This comparison provides insights into the ligand sites involved in chelation, enhancing understanding of the complexation process. A comparison shows that the absorption bands in the FTIR spectra of the ligand change during the chelation process, as shown in Table 1 and Figure 3. The coordination of this ligand with the metal ions and the deposition of theC=N¯ and O−H-bearing azomethane imine group changes its position and intensity or shape in relation to the ligands (L). Thus, the entire complex is usually represented in the spectral band. Broad bands representing υ =C−H stretching frequencies, such as υ (3100–3500) cm^{-1}, were observed for the synthesized complexes and a moving fast track with the movement of water or decomposed particles (Abdulghani and Khaleel, 2013; González-García et al., 2016; Nakamoto, 2009). In the spectra of the complexes, additional vibrational modes are observed due to the bonding of the metal ions with the ligands. These vibrations are related to the frequencies of the ligand and are within the range of 524–561 cm^{-1} for υ (M-N) and 401–482 cm^{-1} for υ (M-O) (Salavati-Niasari et al., 2008). FTIR analysis was used to further the structural characterization of the Co_3O_4 and ZnO NPs. Co_3O_4 NPs showed characteristic Co–O vibrational modes at 580 cm^{-1} and 670 cm^{-1}, attributed toCo–O bonds and bridging O bonds to Co, respectively. The FTIR spectra of the synthesized ZnO NPs showed Zn–O vibrations at 474 cm^{-1}.

3.2 Electronic Spectra $Co(HBZAP)(OAC)_2]2H_2O$,$[Zn(HBZAP)(OAC)_2]H_2O$ Complexes

The ultraviolet-visible (UV-vis) spectra of [Co(Schiff base)$(OAC)_2]2H_2O$ and [Zn(Schiff base)$(OAC)_2]2H_2O$ complexes could reveal information on their electronic structure, ligand field, and geometry. Figure 4 and Table 2 show the electronic spectra, magnetic susceptibility, and atomic percentage for the ligand and metal–ion complexes (Bain and Berry, 2008; Jyothi et al., 2022; Pavia et al., 2014).

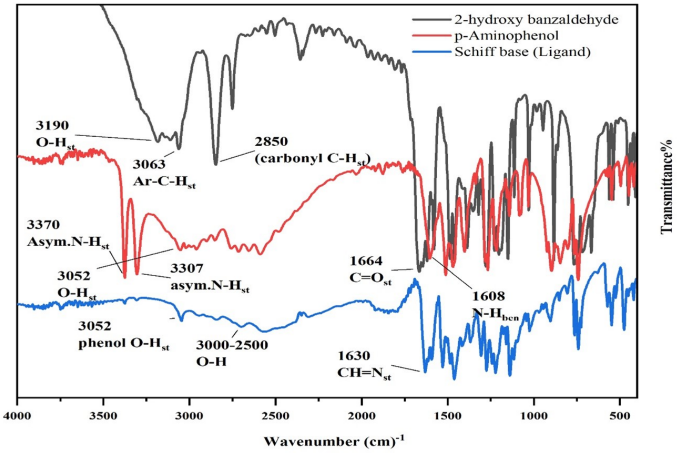

Figure 2. FTIR Characterizations for Chemical Reagents (2-Hydroxybenzaldehyde, p-Aminophenol) and N-(2-Hydroxybenzylidene)-4-Aminophenol (HBZAP)

3.3 ^{1}H-NMR Spectra N-(2-Hydroxybenzylidene)-4-Aminophenol (HBZAP), $[Co(HBZAP)(OAC)_2]2H_2O$,$[Zn(HBZAP)(OAC)_2]$ H_2O Complexes

The ^{1}H-NMR spectra of N-(2-Hydroxybenzylidene)-4-aminophenol (HBZAP), $[Co(C_{13}H_{11}NO_2)(OAc)_2]2H_2O$ and $[Zn(C_{13}H_{11}NO_2)(OAc)_2]2H_2O$ complexes were acquired in deuterated dimethyl sulfoxide (DMSO-d6) to investigate the structural and electronic modifications resulting from metal coordination. A comparative analysis of the spectra Figure 5 shows distinct coordination-induced shifts and peak broadening, which directly correlated with changes in the proton environment of the ligands upon metal binding. The ligand showed phenolic group signals at δ 9.7 and 13.7 ppm and a peak for imine proton at δ 8.9 ppm, in addition to the aromatic protons at δ 6.8–7.6 ppm (Silverstein et al., 2005).

^{1}H-NMR spectral studies of paramagnetic Co (II) Schiff base complexes typically show peaks that have broadened and shifted due to the paramagnetic nature of Co (II). This broadening results from the interactions between the paramagnetic center and the nuclear spins. The unpaired electrons on the metal interact with the nuclear spins of the protons, leading to rapid relaxation times (Dhale et al., 2023; Pettersen et al., 2004). Upon coordination with Zn (II), this proton may experience a slight shift, often moving upfield (lower ppm) due to the electron-donating effect of the metal, which increases the electron density around the nitrogen. A pronounced downfield shift of the azomethine proton resonance (−CH=N−) to 7.5 ppm in the Zn(II) complex spectrum (compared to the free ligand) provides unequivocal spectroscopic evidence for the coordination of the imine nitrogen to the metal center. This deshielding effect arises from electron density withdrawal by Zn (II) through the σ-bonding framework, consistent with a metal-imine covalent interaction. Furthermore, the free ligand

Table 1. FTIR Spectra: Reagents (2-Hydroxybenzadehyde, 4-Aminophenol), Ligand-Metal Complexes, and Characterization of the Metal Oxide NPs

Compound	v(C=O) cm^{-1}	v(NH2) Asym-sym cm^{-1}	v(CH=N) cm^{-1}	v(O-H) cm^{-1}	v(M-N) cm^{-1}	v(M-O) cm^{-1}
2-hydroxybenzaldehyde	1664	-	-	3182	-	-
4-aminophenol	-	3354–3294	-	-	-	-
Schiff base ligand	-	-	1631	3095	-	-
[Co(HBZAP)(OAC)2]2H2O	-	-	1604	-	425	458
Zn(HBZAP)(OAC)2]	-	-	1614	-	420	460
H_2O			-	-	-	
CoO						580
OCoO bridging						670
ZnO NPs						474

Table 2. Electronic Data Spectra, Magnetic Susceptibility, and Atomic Percentages for N-(2-Hydroxybenzylidene)-4-Aminophenol (HBZAP), (b) $[Co(HBZAP)(OAC)_2]2H_2O$,$[Zn(HBZAP)(OAC)_2]H_2O$ Complexes

$Zn(HBZAP)(OAC)_2]\ H_2O$	Absorption Bands (nm)	Assignments	μ_{eff} B.M. (Cal.)	Metal % (Cal.)	Suggested Geometry
Schiff base ligand	270	$n\rightarrow\pi^*$	-	-	-
	348	$\pi\rightarrow\pi^*$			
	433	$n\rightarrow\pi^*$			
$[Co(HBZAP)(OAC)_2]2H_2O$	426	$^4A_2$ (F)$\rightarrow$ $^3T_2$ (F)	2.99	11.97	Tetrahedral
	533	$^4A_2$ (F)$\rightarrow^3T_2$ (p)	(2.82)	(13.86)	
	237	MLCT		(12.3)	
	267	MLCT			
$Zn(HBZAP)(OAC)_2]\ H_2O$	418	MLCT	0	13.75	
	447	MLCT		(15.08)	

exhibited a distinct resonance at 13.7 ppm, assigned to the hydroxyl proton (OH) of the phenolic or enolic moiety (Mishra et al., 2018).

3.4 ^{13}C-NMR Spectral Characterization for N-(2-Hydroxybenzylidene)-4-Aminophenol (HBZAP)

^{13}C-NMR spectroscopy is used to investigate the carbon atoms in a compound, providing information about the types of carbon atoms present and the chemical environments they inhabit. In the case of Schiff base ligands, the ^{13}C-NMR spectrum offers valuable insights into the structure and chemical properties of the ligand. The chemical shift values indicate the shifts of the carbon atoms in the Schiff base ligand. These chemical shifts are reported in Table 3 and Figure 6, expressed in (ppm) relative to an internal standard, typically tetramethylsilane (TMS). The dramatic shift of these carbon atoms in the Schiff base ligands provides information on various properties of the ligand, such as the chemical environment and the structure (Silverstein et al., 2005).

3.5 Characterizations of Cobalt and Zinc Oxide NPs

3.5.1 XRD of Cobalt and Zinc Oxide NPs

The sharpness and intensity of the peaks in the XRD pattern of the $[Co(C_{13}H_{11}NO_2)(OAc)_2]2H_2O$ complex Figure 7 indicate the crystalline nature of the complex. The 2θ values of the peaks were indexed to find the lattice parameters and the tetragonal crystal structure (El-Gammal et al., 2021). The peaks in the XRD pattern of Co_3O_4 are shown in Figure 6: 19.10°, 31.25°, 36.90°, 44.90°, 55.65°, 59.40°, 65.25°, and 77.45°. These peaks were compared with standard reference data for Co_3O_4, such as those available in the Joint Committee on Powder Diffraction Standards (JCPDS card (98-006-9365)) database (Lin et al., 2016). Co_3O_4 has a cubic symmetry, characterized by a few symmetric peaks, unlike the Schiff base complexes, which have lower symmetry (Razmara and Janczak, 2021). However, specific diffraction patterns that correspond to its cubic crystalline phase can be used to index these peaks to the appropriate Miller indices: (111), (022), (113), (222), (004), (224), (115), (044), and (335) (Boureguig et al., 2020). The average crystallite size, 36.65 nm, was determined using the Debye–Scherrer Equation (2) to estimate the crystallite size:

Table 3. ^{13}C-NMR Characterization of N-(2-Hydroxybenzylidene)-4-Aminophenol (HBZAP)

C/H	Chemical Shift (δ)ppm	Interpretation	References
$-C-OH_8$	161	due to OH from salicylaldehyde	(Bader et al., 2019; Silverstein et al., 2005)
$-C-OH_{16}$	154	due to OH from p-aminophenol	(Bader et al., 2020)
$-CH=N_7$	160	due to formation of imine group C=N for Schiff base	(Al-Qasii et al., 2023)
(C-aromatic)$C_{13}-C_{17}$	114-144	due to aromatic carbons	(Silverstein et al., 2005)
δ(DMSO)	40	DMSO	(Silverstein et al., 2005)

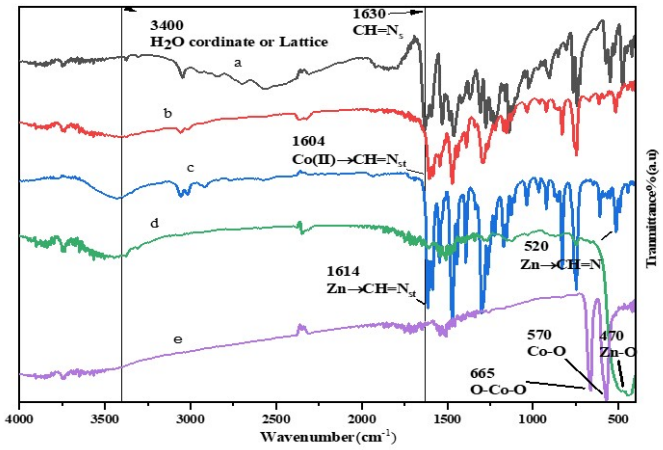

Figure 3. FTIR Spectral Analyses for (a) N-(2-Hydroxybenzylidene)-4-Aminophenol (HBZAP), (b) [Co(HBZAP)(OAC)$_2$]2H$_2$O ,[Zn(HBZAP)(OAC)2] H2O complexes, (d) Co_3O_4, and (e) ZnO nanoparticles

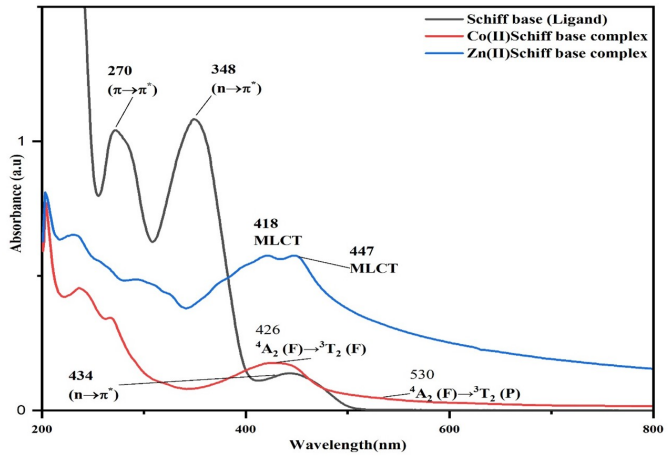

Figure 4. Electronic Spectra for N-(2-Hydroxybenzylidene)-4-Aminophenol (HBZAP), (b) [Co(HBZAP)(OAC)$_2$]2H$_2$O ,[Zn(HBZAP)(OAC)$_2$] H$_2$O Complexes

$$x = \frac{k\lambda}{\beta cos(\theta)} \quad (2)$$

where: D is the average crystallite size, $K$is the dimensionless Scherrer constant ($K \approx 0.9$ for spherical crystallites), λ is the X-ray wavelength nm (typically 0.154 nm for Cu-$K\alpha$ radiation), β is the full width at half maximum (FWHM) of the diffraction peak, θ is the Bragg angle (in radians) These peaks were at the expected positions for Co_3O_4, confirming the cubic spinel structure of Co_3O_4 (Matinise et al., 2018).

Similarly, X-ray powder diffraction analysis was performed for the polycrystalline material of the coordinated complex. The XRD patterns of these complexes indicated a well-defined crystalline structure Figure 8 for the [Zn($C_{13}H_{11}NO_2$)(OAc)$_2$] 2H$_2$O complex, which indicated a cubic crystal system. The average grain size was calculated as 22.8 nm using the Debye–Scherrer formula. In the case of ZnO NPs, the typical XRD pattern of ZnO NPs exhibited several characteristic peaks, which were indexed to the hexagonal wurtzite crystal structure according to JCPDS No. 36–1451 (Sutharappa Kaliyamoorthy et al., 2022). In general, the most prominent peaks are observed at 31.8°, 34.4°, 36.3°, 47.5°, 56.6°, and 62.9°, which correspond to the (100), (002), (101), (102), (110), and (103) crystal planes (Katouah, 2021). The crystallite size of the ZnO was calculated using the Debye–Scherrer Equation (2), yielding an average value of 31.9 nm.

3.6 Field Emission Scanning Electron Microscopy (FESEM) Characterization of Co_3O_4 and ZnO

Field emission scanning electron microscopy (FESEM) offers higher resolution and superior surface detail than conventional SEM, making it an excellent choice for analyzing Co_3O_4 and ZnO NPs (Lewczuk and Szyryńska, 2021). FESEM provides a detailed understanding of NP morphology and size distribution when combined with size distribution analysis (Bin Mobarak et al., 2022). By employing appropriate sample preparation, imaging, and analysis techniques, comprehensive insights into

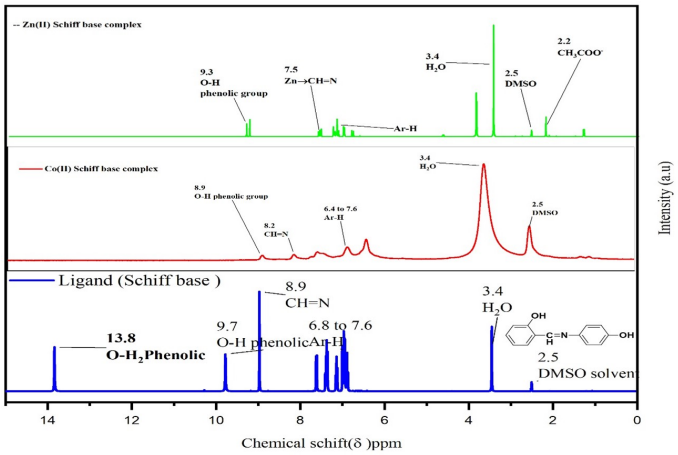

Figure 5. ^{1}H-NMR Spectral Characterizations N-(2-Hydroxybenzylidene)-4-Aminophenol (HBZAP), $Co(C_{13}H_{11}NO_2)(OAc)_2]2H_2O$ and $[Zn(C_{13}H_{11}NO_2)(OAc)_2]2H_2O$ Complexes

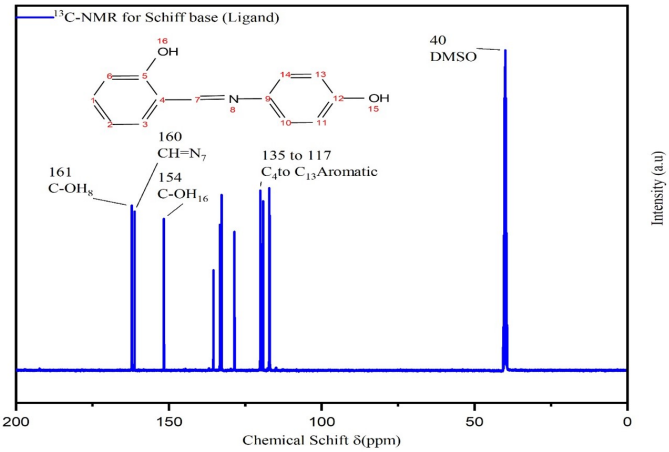

Figure 6. ^{13}C-NMR Spectral Characterization for N-(2-Hydroxybenzylidene)-4-Aminophenol (HBZAP)

the structural properties of these NPs can be obtained. Such insights are crucial for the application of the NPs in various fields.

The morphology of theCo_3O_4 NPs was analyzed using FE-SEM, as shown in Figure 9a. The low-magnification FESEM image in Figure 9b reveals that many Co_3O_4 NPs are uniformly distributed over the nanosheets. The high-magnification FE-SEM images demonstrate two sizes of Co_3O_4 NPs, small and large, on the surface (Figure 9c and inset). The diameter of the Co_3O_4 NPs was measured using the ImageJ software (1.53v) and represented as a histogram, as shown in Figure 9. The Co3O4 NPs have an average size of about 55 nm.

3.7 Optical Absorption and Band Gaps of Co_3O_4 and ZnO

The optical absorption spectra of the Co_3O_4 and ZnO NPs generally contain discernible peaks that correspond to electronic transitions across the material that provide insights into the electronic structures and band gaps of these particles. Co_3O_4 NPs typically exhibit absorption in the UV-visible range. The major absorption Figure 9 peaks observed at 447 nm and 733 nm can be attributed to charge transfer transitions from O^{2-} to Co^{2+} and $O^{-2} \rightarrow Co^{3+}$, respectively (Makhlouf et al., 2013). Co_3O_4 was measured in water using a UV-Vis spectrophotometer based on the Tauc relation with Equation (3).

$$\varepsilon hv = P(Eg - hv) \quad (3)$$

where: ε represents the molar extinction coefficient, h is Planck's constant, v corresponds to the frequency of light, Eg is the bandgap energy, p is a constant. The plot of $(\varepsilon hv)^2$ versus the photon energy (hv) shows a distinct absorption edge for the powdered catalyst. The bandgap energy (Eg) was calculated by extrapolating the linear region of the plot, as shown

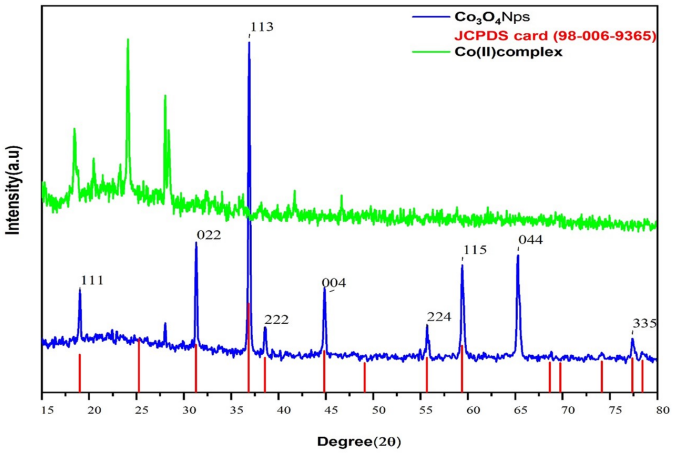

Figure 7. XRD Patterns of a $[Co(HBZAP)(OAC)_2]2H_2O$ Complex andCo_3O_4 NPs

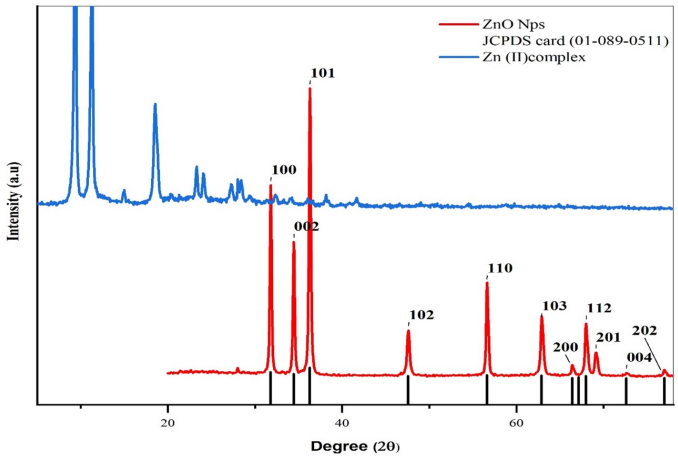

Figure 8. XRD Patterns of a $[Zn(C_{13}H_{11}NO_2)(OAc)_2]2H_2O$ Complex and ZnO NPs

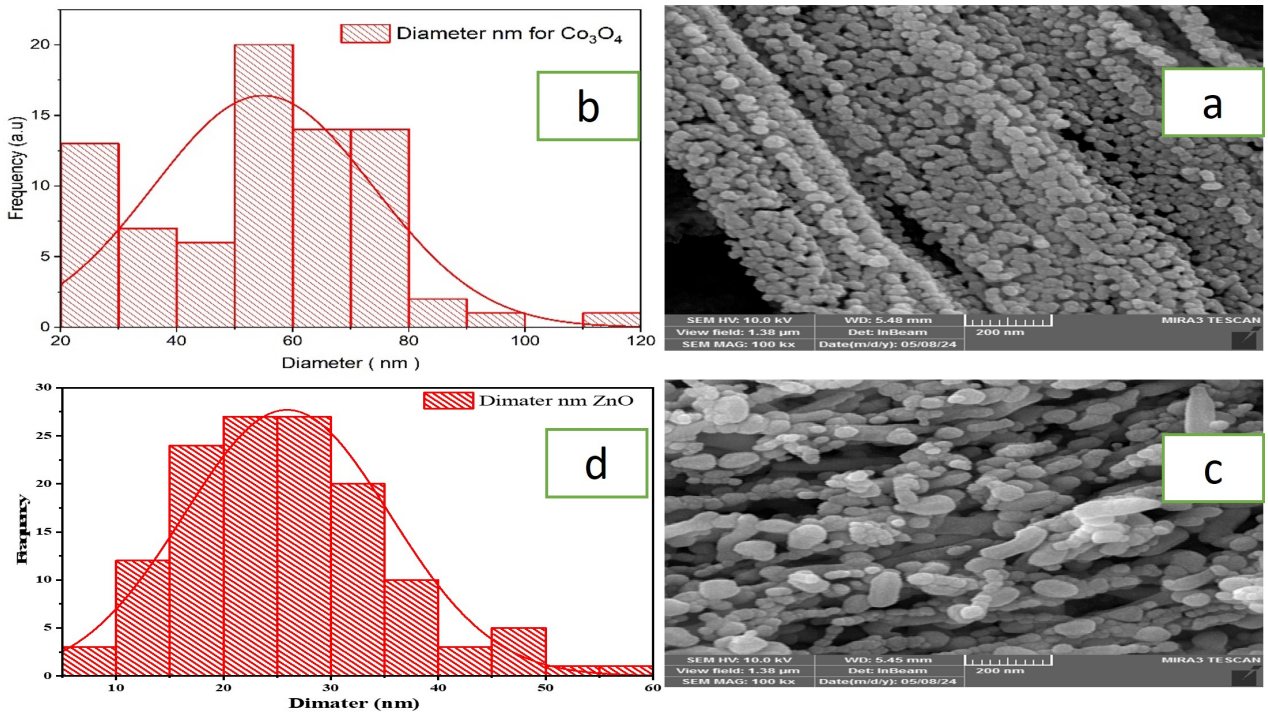

Figure 9. (a,c) FESEM Images and (b,d) Size Histograms for $Co_3O_4$and ZnO Nanoparticles

in Figure 10. The direct bandgap (*Eg*) is size-dependent, as expected from the quantum confinement effect, which causes the bandgap of a semiconductor to increase as the particle size decreases. Co_3O_4 has a spinel structure composed of Co^{2+} and Co^{3+} ions; therefore, its electronic properties are unique. The mixture of two cobalt ions yields two different electronic transitions and corresponding band gaps (Debanath and Karmakar, 2013; Xu et al., 2016). The calculated direct band gaps for the Co_3O_4 NPs are 1.57 and 1.95 eV because it is a mixed-valence compound with a complex electronic structure. Similarly, the absorption spectrum of ZnO nanopowder is shown in Figure 11. It shows a strong absorption band around 362 nm, assigned to the ZnO NPs. There is no significant difference between this wavelength and the bandgap wavelength of 362 nm (*Eg* = 3.2 eV) (Lopes de Almeida et al., 2021).

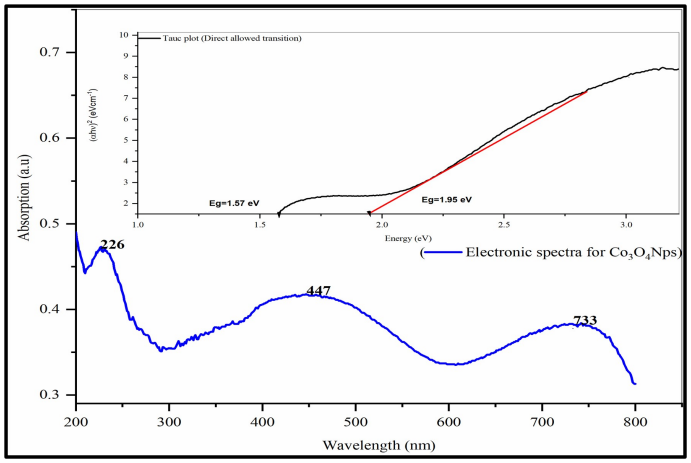

Figure 10. Electronic Transitions and Tauc Plot (direct allowed transition) for Co_3O_4NPs

3.8 Photodegradation of CR Dye

CR dye, a toxic industrial effluent, is carcinogenic, and much effort has been made to degrade it through semiconductor photocatalysis. Recent reports (Gaur et al., 2023; Magdalane et al., 2019) have shown the photocatalytic degradation of CR dye by Co_3O_4 and ZnO nano-heterostructures with a degradation efficiency of 95%. Other similar nanocomposite photocatalysts have been reported, which showed higher photocatalytic degradation efficiencies of 90% and 94%. The photocatalytic efficiency of the prepared Co_3O_4 and ZnO NPs was evaluated in comparison with the standard ZnO NPs used as a photocatalyst. The prepared samples were found to be suitable for environmental applications. The metal oxide NPs were used for the photocatalytic treatment of CR through UV light irradiation for 1 hour. The UV-Vis spectra of the reactant solutions at different irradiation periods were collected with an absorbance meter at 25°C to identify the absorbance of the reactant solutions, and the percentage photocatalytic decomposition was calculated from the change in absorbance after a given time using the UV-Vis spectra.

The potential mechanism of CR degradation in the presence of ZnO particles under UV illumination is as follows: an electron (e^-) absorbs energy and is excited from the valence

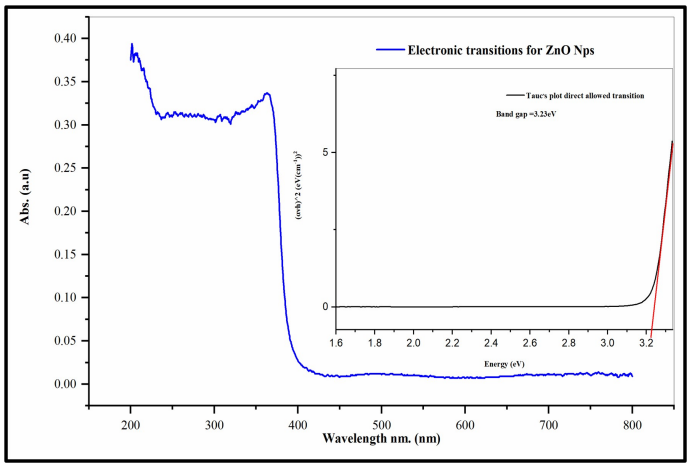

Figure 11. Electronic Transitions and Tauc Plot (direct allowed transition) for ZnO NPs

band (VB) to the conduction band (CB) of the MO; this leaves a hole (h+) in the valence band (VB) of the MO. Consequently, an e^-–h+ pair separates; this creates an active radical species, which is responsible for the degradation of the dye.

3.8.1 Photoeffect of Initial Dye Concentration

The initial concentration of the CR dye was varied (30-60 ppm), while the catalyst loading constant (0.1 g/100 mL) remained the same to investigate the impact of the initial concentration on the degradation rate. The results, presented in Figure 12, show a linear relationship between the normalized dye concentration and the irradiation time during the photocatalytic degradation of the dye. Furthermore, the results presented in Figure 13 suggest that the initial concentration of the dye influences its degradation rate. The dye degradation rate drops significantly for dye concentrations above this critical value.

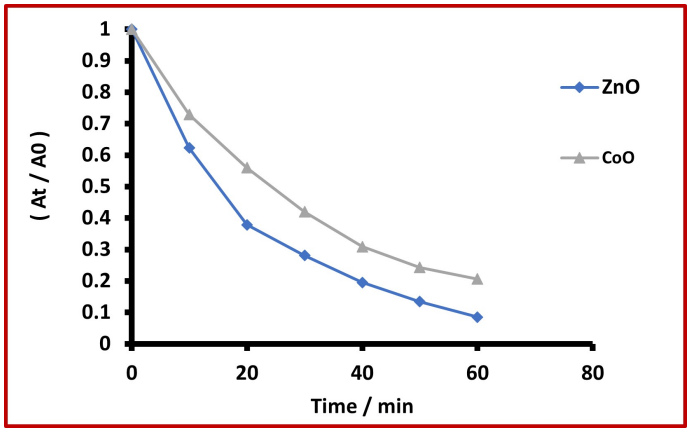

Figure 12. Effect of Initial Concentration on Dye Degradation Using ZnO and Co_3O_4 as the Catalyst

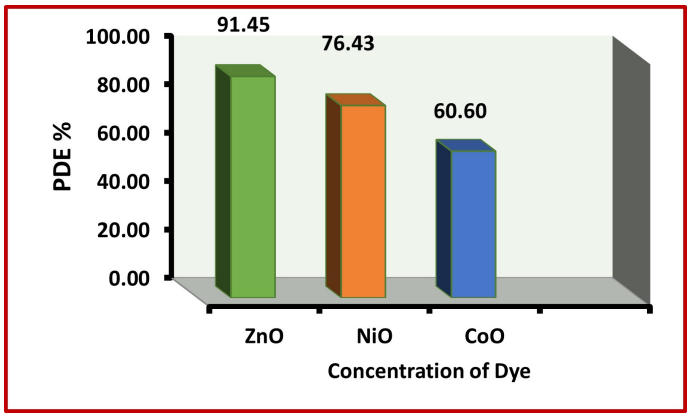

Figure 13. Photodegradation Efficiency (PDE%) of ZnO and Co_3O_4 for Dye Degradation

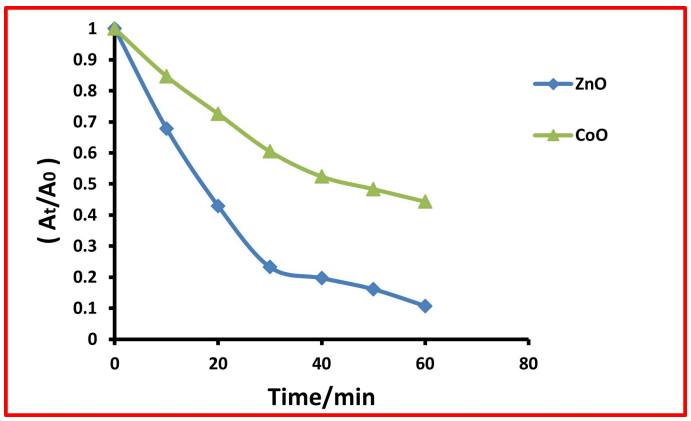

Figure 14. Variation in (At / A0) With Irradiation Time

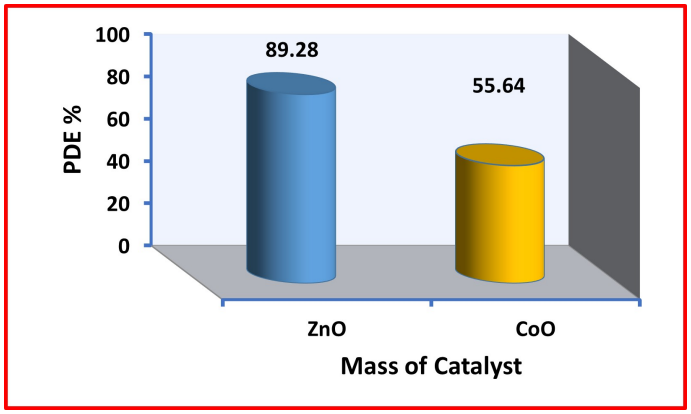

Figure 15. Photocatalytic Degradation Efficiency Using 0.1 g / 100 ml ZnO and Co_3O_4 NPs Against Different Concentrations of Congo Red Dye

3.8.2 Effect of Catalyst Loading

To systematically evaluate the influence of initial dye concentration on the photocatalytic degradation kinetics, a series of experiments were conducted under constant catalyst loading

(0.1 g/100 mL) while varying the dye concentration from 30 to 60 ppm. Figure 14 shows the evolution of the normalized dye concentration (C/Co) as a function of irradiation time, revealing distinct pseudo-first-order degradation kinetics across lower concentrations (30–50 ppm). However, as shown in Figure 15, a marked deviation from this trend occurs at higher concentrations (>50 ppm), where the apparent rate constant (kobs) decreases significantly.

4. CONCLUSIONS

New N-(2-Hydroxybenzylidene)-4-aminophenol),and their $Co(C_{13}H_{11}NO_2)(OAc)_2]2H_2O$ and $[Zn(C_{13}H_{11}NO_2)(OAc)_2]2H_2O$ complexes were prepared and characterized. These complexes were used to prepare Co_3O_4 and NiO NPs, which display excellent photocatalytic activity in CR degradation. The adsorption efficiency of the ZnO NPs for removing CR dye was better than that of Co_3O_4. Increasing the amount of catalyst used increased the PDE after reaching optimum conditions. Increasing the Congo red dye concentration decreased the photodegradation rate but, at the same time, reduced the degradation efficiency. The prepared oxide NPs exhibited elevated photocatalytic activity toward the decomposition of the CR dye under UV irradiation. The degradation rates for CR dye were 91.4% and 60.4% at 60 min for ZnO and Co_3O_4, respectively.

5. ACKNOWLEDGMENT

The authors wish to express their appreciation to Dr. Hazim Al-Jubury, Lec. Mohammed Al-Majidi, and the Faculty of Women for Scientific Disciplines at the University of Babylon, Iraq, for providing the resources and support needed to complete this study.

REFERENCES

Abass, S. K., J. A. Al-Hilfi, S. K. Abbas, and L. M. Ahmed (2020). Preparation, Characterization and Study of the Photodecolorization of Mixed-Ligand Binuclear Co (II) Complex of Schiff Base by ZnO. *Indonesian Journal of Chemistry*, **20**(2); 404–412

Abdallah, S. M., G. G. Mohamed, M. Zayed, and M. S. Abou El-Ela (2009). Spectroscopic Study of Molecular Structures of Novel Schiff Base Derived from O-Phthaldehyde and 2-Aminophenol and Its Coordination Compounds Together with Their Biological Activity. *Spectrochimica Acta Part A: Molecular and Biomolecular Spectroscopy*, **73**(5); 833–840

Abdelrahman, E. A. and E. S. Al-Farraj (2022). Facile Synthesis and Characterizations of Mixed Metal Oxide Nanoparticles for the Efficient Photocatalytic Degradation of Rhodamine B and Congo Red Dyes. *Nanomaterials*, **12**(22); 3992

Abdulghani, A. J. and A. M. N. Khaleel (2013). Preparation and Characterization of Di-, Tri-, and Tetranuclear Schiff Base Complexes Derived from Diamines and 3,4-Dihydroxybenzaldehyde. *Bioinorganic Chemistry and Applications*, **2013**; 1–10

Adaji, M., M. Iorungwa, and O. Salawu (2024). Characterization of Schiff Base Ligand and Its Metal Complexes. In *Proceedings of the International Conference on Chemistry and Chemical Engineering*

Al-Qasii, N. A. R., A. T. Bader, and Z. Mosaa (2023). Synthesis and Characterization of a Novel Azo-Dye Schiff Base and Its Metal Ion Complexes Based on 1,2,4-Triazole Derivatives. *Indonesian Journal of Chemistry*, **23**(6); 1555–1566

Al-Wasidi, A. S., I. I. S. AlZahrani, H. I. Thawibaraka, and A. M. Naglah (2022). Facile Synthesis of ZnO and Co_3O_4 Nanoparticles by Thermal Decomposition of Novel Schiff Base Complexes: Studying Biological and Catalytic Properties. *Arabian Journal of Chemistry*, **15**(2); 103628

Ashraf, M. A., K. Mahmood, A. Wajid, M. J. Maah, and I. Yusoff (2011). Synthesis, Characterization and Biological Activity of Schiff Bases. In *International Proceedings of Chemical, Biological and Environmental Engineering*, volume 10. page 185

Bader, A. T., B. I. Al-Abdali, and I. K. Jassim (2019). Synthesis and Characterization of New (2-(((5-(3,5-Dinitrophenyl)-1,3,4-Thiadiazol-2-yl-2,5 Dihydroxy Benzalidine))) Metal Complexes. *Journal of Global Pharma Technology*, **11**(5); 39–55

Bader, A. T., N. A. Rasheed, M. Aljeboree, and A. F. Alkaim (2020). Synthesis and Characterization of New 5-(4-Nitrophenyl)-4-((4 Phenoxybenzylidene)Amino)-4H-1,2,4-Triazole-3-Thiol Metal Complexes and Study of the Antibacterial Activity. *Journal of Physics: Conference Series*. Presented at the Journal of Physics: Conference Series

Bain, G. A. and J. F. Berry (2008). Diamagnetic Corrections and Pascal's Constants. *Journal of Chemical Education*, **85**(4); 532–536

Bin Mobarak, M., M. S. Hossain, F. Chowdhury, and S. Ahmed (2022). Synthesis and Characterization of CuO Nanoparticles Utilizing Waste Fish Scale and Exploitation of XRD Peak Profile Analysis for Approximating the Structural Parameters. *Arabian Journal of Chemistry*, **15**(10); 104117

Boureguig, K., H. Tabet-Derraz, and T. Seddik (2020). Insight into Structural, Optical and Electrical Properties of Cobalt Oxide (Co_3O_4) Thin Film. *Surface Review and Letters*, **27**(04); 1950134

Dao, T. T., T. Le Na Vo, A. T. Duong, D. T. Tran, D. L. Nguyen, V. V. Pham, and H. T. Nguyen (2023). Highly Photocatalytic Activity of pH-Controlled ZnO Nanoflakes. *Optical Materials*, **140**; 113865

Debanath, M. K. and S. Karmakar (2013). Study of Blueshift of Optical Band Gap in Zinc Oxide (ZnO) Nanoparticles Prepared by Low-Temperature Wet Chemical Method. *Materials Letters*, **111**; 116–119

Dhale, P. C., P. A. Ubale, K. D. Sonawane, N. M. Naik, M. Afzal, L. A. Ghule, and S. H. Gaikwad (2023). New Triazole-Based Schiff Base Ligands and Their Co(II) and Ni(II) Complexes as Biological Potent Molecules: Chemical Preparation, Structural Elucidation and Biological Studies. *Results in Chemistry*, **6**; 101155

El-Gammal, O. A., F. S. Mohamed, G. N. Rezk, and A. A. El-Bindary (2021). Synthesis, Characterization, Catalytic, DNA Binding and Antibacterial Activities of Co(II), Ni(II) and Cu(II) Complexes with New Schiff Base Ligand. *Journal of Molecular Liquids*, **326**; 115223

Gaur, J., K. Vikrant, K.-H. Kim, S. Kumar, M. Pal, R. Badru, and J. Momoh (2023). Photocatalytic Degradation of Congo Red Dye Using Zinc Oxide Nanoparticles Prepared Using *Carica papaya* Leaf Extract. *Materials Today Sustainability*, **22**; 100339

González-García, C., A. Mata, F. Zani, M. A. Mendiola, and E. López-Torres (2016). Synthesis and Antimicrobial Activity of Tetradentate Ligands Bearing Hydrazone and/or Thiosemicarbazone Motifs and Their Diorganotin (IV) Complexes. *Journal of Inorganic Biochemistry*, **163**; 118–130

Jyothi, P., V. Sumalatha, and D. Rajitha (2022). Cobalt (II) Complexes with N-Methyl Thiosemicarbazide Schiff Bases: Synthesis, Spectroscopic Investigation, Cytotoxicity, DNA Binding and Incision, Anti-Bacterial and Anti-Fungal Studies. *Inorganic Chemistry Communications*, **145**; 110029

Katouah, H. A. (2021). Facile Synthesis of Co_3O_4 and ZnO Nanoparticles by Thermal Decomposition of Novel Co(II) and Zn(II) Schiff Base Complexes for Studying Their Biological Properties and Photocatalytic Degradation of *Crystal Violet* Dye. *Journal of Molecular Structure*, **1241**; 130676

Kumar, A., M. Moradpour, M. Losito, W.-T. Franke, S. Ramasamy, R. Baccoli, and G. Gatto (2022). Wide Band Gap Devices and Their Application in Power Electronics. *Energies*, **15**(23); 9172

Lewczuk, B. and N. Szyryńska (2021). Field-Emission Scanning Electron Microscope as a Tool for Large-Area and Large-Volume Ultrastructural Studies. *Animals*, **11**(12); 3390

Lin, Y., H. Ji, Z. Shen, Q. Jia, and D. Wang (2016). Enhanced Acetone Sensing Properties of Co_3O_4 Nanosheets with Highly Exposed (111) Planes. *Journal of Materials Science: Materials in Electronics*, **27**

Lopes de Almeida, W., N. S. Ferreira, F. S. Rodembusch, and V. Caldas de Sousa (2021). Study of Structural and Optical Properties of ZnO Nanoparticles Synthesized by an Eco-Friendly Tapioca-Assisted Route. *Materials Chemistry and Physics*, **258**; 123926

Magdalane, C. M., K. Kaviyarasu, M. V. Arularasu, K. Kanimozhi, and G. Ramalingam (2019). Structural and Morphological Properties of Co_3O_4 Nanostructures: Investigation of Low Temperature Oxidation for Photocatalytic Application for Waste Water Treatment. *Surfaces and Interfaces*, **17**; 100369

Mahadevi, P. and S. Sumathi (2023). Schiff Base Metal Complexes: Synthesis, Optoelectronic, Biological Studies, Fabrication of Zinc Oxide Nanoparticles and Its Photocatalytic Activity. *Results in Chemistry*, **6**; 101026

Makhlouf, S. A., Z. H. Bakr, K. I. Aly, and M. S. Moustafa (2013). Structural, Electrical and Optical Properties of Co_3O_4 Nanoparticles. *Superlattices and Microstructures*, **64**; 107–117

Matinise, N., N. Mayedwa, X. Fuku, N. Mongwaketsi, and M. Maaza (2018). Green Synthesis of Cobalt (II, III) Oxide Nanoparticles Using *Moringa oleifera* Natural Extract as High Electrochemical Electrode for Supercapacitors. *AIP Conference Proceedings*, **1962**

Mishra, D. K., U. K. Singha, A. Das, S. Dutta, P. Kar, A. Chakraborty, and B. Sinha (2018). DNA Binding, Amelioration of Oxidative Stress, and Molecular Docking Study of Zn(II) Metal Complex of a New Schiff Base Ligand. *Journal of Coordination Chemistry*, **71**(14); 2165–2182

Naikoo, G. A., M. A. S. Tabook, B. A. M. Tabook, M. Bano, I. U. Hassan, R. A. Dar, and T. A. Saleh (2024). Electrochemical Performance of Co_3O_4/Ag/CuO Electrodes for Supercapacitor Applications. *Journal of Energy Storage*, **85**; 111047

Nakamoto, K. (2009). *Infrared and Raman Spectra of Inorganic and Coordination Compounds, Part B: Applications in Coordination, Organometallic, and Bioinorganic Chemistry*. John Wiley & Sons

Nassar, M. Y., H. M. Aly, E. A. Abdelrahman, and M. E. Moustafa (2017). Synthesis, Characterization, and Biological Activity of Some Novel Schiff Bases and Their Co(II) and Ni(II) Complexes: A New Route for Co_3O_4 and NiO Nanoparticles for Photocatalytic Degradation of Methylene Blue Dye. *Journal of Molecular Structure*, **1143**; 462–471

Nwaiwu, B. C., E. E. Oguzie, and C. C. Ejiogu (2024). Photocatalytic Degradation of Congo Red Using Doped Zinc Oxide Nanoparticles. *EQA-International Journal of Environmental Quality*, **60**; 18–26

Patil, M., V. Masand, and A. Maldhure (2020). Schiff Base Metal Complexes Precursor for Metal Oxide Nanomaterial: A Review. *Current Nanoscience*, **16**

Pavia, D. L., G. M. Lampman, G. S. Kriz, and J. A. Vyvyan (2014). *Introduction to Spectroscopy*. Cengage Learning

Pettersen, E. F., T. D. Goddard, C. C. Huang, G. S. Couch, D. M. Greenblatt, E. C. Meng, and T. E. Ferrin (2004). UCSF Chimera—A Visualization System for Exploratory Research and Analysis. *Journal of Computational Chemistry*, **25**(13); 1605–1612

Pushpanathan, V. and D. Suresh Kumar (2014). A Novel Zinc (II) Macrocycle-Based Synthesis of Pure ZnO Nanoparticles. *Journal of Nanostructure in Chemistry*, **4**; 95–101

Razmara, Z. and J. Janczak (2021). Sonochemical Synthesis and Structural Characterization of a New Three Mono-Nuclear Cobalt(II) Complex, to Produce Tricobalt Tetroxide as an Effective Heterojunction Catalyst. *Journal of Molecular Structure*, **1229**; 129500

Saeed, M., H. M. Marwani, U. Shahzad, A. M. Asiri, and M. M. Rahman (2024). Recent Advances, Challenges, and Future Perspectives of ZnO Nanostructure Materials Towards Energy Applications. *The Chemical Record*, **24**(1); e202300106

Salavati-Niasari, M., F. Davar, and M. Mazaheri (2008). Preparation of ZnO Nanoparticles from [Bis (Acetylacetonato)

Zinc (II)]–Oleylamine Complex by Thermal Decomposition. *Materials Letters*, **62**(12-13); 1890–1892

Silverstein, R. M., F. X. Webster, and D. J. Kiemle (2005). *Spectrometric Identification of Organic Compounds*. Wiley

Singh, V. and D. Major (2016). Electronic Structure and Bonding in Co-Based Single and Mixed Valence Oxides: A Quantum Chemical Perspective. *Inorganic Chemistry*, ***55***

Subhi, H. M., A. T. Bader, and H. Y. Al-Gubury (2022). Synthesis and Characterization of ZnO Nanoparticles via Thermal Decomposition for Zn(II) Schiff Base Complex. *Indonesian Journal of Chemistry*, **22**(5); 1396–1406

Sutharappa Kaliyamoorthy, T., V. Subramaniyan, S. Renganathan, V. Elavarasan, J. Ravi, P. Prabhakaran Kala, and S. Vijayakumar (2022). Sustainable Environmental-Based ZnO Nanoparticles Derived from *Pisonia grandis* for Future Biological and Environmental Applications. *Sustainability*, **14**(24); 17009

Xu, L., Q. Jiang, Z. Xiao, X. Y. Li, J. Huo, S. Y. Wang, and L. M. Dai (2016). Plasma-engraved Co_3O_4 nanosheets with oxygen vacancies and high surface area for the oxygen evolution reaction. *Angew. Chem.*, **128**; 5363–5367

Zhu, H., J. Luo, J. Liang, G. Rao, J. Li, J. Y. Zhang, and Z. Du (2008). Synthesis and magnetic properties of antiferromagnetic Co_3O_4 nanoparticles. *Physica B: Condensed Matter*, **403**; 3141–3145

